INTERNATIONAL JOURNAL OF HYDROGEN ENERGY 48 (2023) 37473–37488

Available online at www.sciencedirect.com

ScienceDirect

journal homepage: www.elsevier.com/locate/he

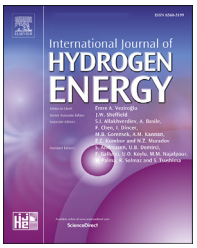

Insights in the application of highly conductive structured catalysts to CO_2 methanation: Computational study

Simona Renda [a,*], *Antonio Ricca* [b], *Vincenzo Palma* [a]

[a] *University of Salerno, Department of Industrial Engineering, Via Giovanni Paolo II 132, 84084 Fisciano (SA), Italy*
[b] *ENEA – Italian National Agency for New Technologies, Energy and Sustainable Economic Development - TERIN-STSN-SGRE, Piazzale Enrico Fermi 1, 80055 Portici, NA, Italy*

HIGHLIGHTS

- Computer-aided simulations allow an in-depth study on structured catalysts applied to exothermic systems.
- Structured catalysts provide for a counter-flux heat conductive transport at low gas velocity.
- The scale-up reduces the advantages in the use of structured catalyst systems.
- The switch to the radial flow geometry is a potential solution for structured catalysts scale-up.

ARTICLE INFO

Article history:
Received 28 October 2022
Received in revised form
5 January 2023
Accepted 27 January 2023
Available online 14 February 2023

Keywords:
CO2 methanation
Computational study
Highly conductive structured catalysts
Heat management
Transport phenomena

ABSTRACT

Nowadays, the optimization of the heat management in highly exothermic processes is a key issue. In recent years, highly conductive structured catalysts have been widely recognized in recent years as a tool for the process intensification of several technologies of this kind. To the best of our knowledge, despite the great availability of studies (both experimental and computational) on the topic, only the potentiality of this application has been discussed so far. Less attention has been paid to the limitations of structured catalysts systems. This work aims to provide an overview on the application of different types of structured catalysts in highly exothermic reactions using as probe reaction the methanation of CO_2, offering a perspective view on the industrialization and scale up of this technology. The transport phenomena of momentum, heat and mass coupled with the chemical reaction have been detailed via computational study and compared to a previous experimental work, highlighting how the potentiality observed on lab scale will lose appeal in a scaled-up configuration, where higher Reynolds numbers are involved. Finally, the study provides a possible solution for the application of structured catalysts on bigger scale, without losing the advantages of thermal conductivity observed in the lab-scale experiments.

* *Corresponding author.*
E-mail address: srenda@unisa.it (S. Renda).

https://doi.org/10.1016/j.ijhydene.2023.01.338

Introduction

Highly conductive materials have been recently introduced in catalysis to the aim of enhancing the heat management issues typical of both exothermic and endothermic reaction systems [1,2]. The importance of optimized heat management is particularly relevant in pursuing a continuous process intensification (PI), as it allows to minimize the size of a reaction unit or to reduce the number of stages of a process, thus leading to more compact and efficient solutions [3]. Usually, conductive materials are used as a carrier for a proper catalytic phase, developing the so-called highly conductive structured catalysts (HCSC) which, in nowadays scenario, pave the way toward process intensification [4,5]. The improved thermal control is one of the most relevant advantages of their application, and impacts on two main aspects: on one hand, these materials allow the obtainment of flatter temperature profiles, leading to the reduction of hot spots and therefore sintering phenomena, and to a restrain of the local thermodynamic limitations [6]. On the other hand, they provide for an easier addition/removal of heat to/from the catalytic bed [7], noteworthily reducing the total costs.

Among the processes in which HCSC can be profitably applied, CO_2 methanation is nowadays particularly studied. The high exothermicity of this reaction (Eq. (1), $\Delta H_{298K-} = -165$ kJ mol^{-1}) produces a significant increase in temperature, leading to several damages to the catalyst and therefore to the efficiency of the process [8,9]. Hence, CO_2 methanation represents an application in which the use of conductive catalysts can offer particularly advantageous improvements [10].

$$CO_2 + 4H_2 \rightleftarrows CH_4 + 2H_2O \quad \text{Eq. 1}$$

In a conventional adiabatic reactor, the system develops a strong temperature increase within a single stage, and therefore it is forced to face the thermodynamic limitation, heading to the necessity of several inter-refrigerated reaction stages to reach high conversion values [11]. Of course, this implies huge reaction volumes and the presence of auxiliary units such as heat exchangers or expensive shell and tube reactor configurations [12,13]. In this context, the substitution of conventional catalysts with highly conductive structured catalysts might allow the CO_2 methanation process intensification [14].

Several studies are reporting the application of structured catalysts to this process, and it is frequently highlighted that the thermal conductivity of the chosen carrier determines the performances of the system [15]. Particular interest was dedicated to micromonoliths, usually made of FeCr-alloy, whose pseudo-gyroid structure is tunable since they can be easily modeled [16,17]. A related controlling factor is the relative density of the carrier within the occupied volume and the coating layer thickness: the higher the former and the lowest the latter, the better the catalytic activity registered for these systems [18]. Furthermore, the morphological characteristics of the carrier play a key role in determining the observed reaction rate, and it has been frequently highlighted that randomly-organized structures or stacked configurations can lead to enhanced activity if compared to channeling configurations [19–21]. A peculiar arrangement of catalytic-coated metallic foils was proposed by Iwaniszyn et al. [22]. An exception is made in case of fast reaction, where honeycombs demonstrated to offer better performances than metal foams [23]. The interest of the scientific community toward the application of structured catalysts to CO_2 methanation encourages the deepening of the research on this topic, to the aim of having a detailed scenario to optimize their eventual industrial application.

Recent attention has also been paid to simulation studies, which allow to deepen the knowledge of phenomena that cannot be observed experimentally, such as punctual variations of a system parameter or non-measurable quantities, such as heat fluxes [24]. In addition, a reliable simulation reduces the cost of experimental evaluations and allow the immediate visualization of the results [25,26]. Simulation results already allowed to understand some peculiar mechanisms of exothermic reactions related to temperature non-uniformities, hot-spot formation and the creation of patterns that are harmful for the operativity of industrial reactors [27–29].

In a previous work, we highlighted the differences between two structured catalytic systems and a conventional powder catalyst, speculating on the possible reasons behind the observed macroscopic effects [30]. In this work, we aim to conduct an in-depth investigation of the mechanisms aside from the chemical reaction, through the employment of the computational fluid dynamic technology (CFD) for the resolution of the complex analytical equations that characterize the transport phenomena. The hypotheses of the precedent work will be corroborated throughout the manuscript, and a further evaluation of the possibility of conveniently employing structured catalysts in scaled-up plants will be discussed.

Model description

This work has been conceived as a detailed investigation on the catalytic and thermal behavior of structured and powder catalysts in CO_2 methanation reaction. It can be divided into two studies: a first evaluation of the transport phenomena taking place along with the methanation reaction in a lab-scale system and a second analysis of the issues related to the application of structured catalysts in scaled-up solutions. In both sections, the work has been conducted with the aid of the simulation software COMSOL Multiphysics. This comes with a pre-built package of physical equations, called physics, grouped based on the described phenomenon.

For the first part of this work, three different catalytic systems were studied and compared: a powder catalyst and two different highly conductive structured catalysts, namely an aluminum open cell foam (40 PPI) and a honeycomb SiC monolith with a flow-through channel configuration. The catalysts formulation, 10 wt% of Ni supported onto an alumina-based washcoat, has been optimized in a previous work, in which the catalytic activity of these systems was also investigated [30]. Based on this preliminary study, the kinetic parameters to be implemented in COMSOL for the simulation of the chemical reaction have been optimized, following the kinetic expressions proposed by Xu and Froment [31]. Based

on the evaluation on the effect of the porosity of aluminum foam on diffusion effect conducted on a previous study [32], the hypothesis of existence of diffusion regime within this system was excluded. To assess the validity of the computational study, geometrical parameters and operating conditions which were characteristic of the previous experimental campaign were completely transferred to the computational study.

For the second part of this work, the hypothesis of scaling up a structured catalyst system (in particular, the aluminum foam) has been analyzed and discussed.

Geometry and domains

Geometry definition is a key aspect of the model: COMSOL allows to build up the geometry in different domains, to which the physics can be selectively applied. The geometry defined for the models is a detailed representation of the experimental setup. The system was constituted by a quartz reactor (ID 22 mm and 400 mm long) horizontally located in an electrical furnace for the temperature control. The catalyst (either the powder catalyst, the aluminum foam, or the SiC monolith) was located in the middle of the reactor and held by two quartz wool disks to avoid powder entrainment and to enhance the gas flow uniformity across the catalytic bed sections [33]. Then, it was surrounded by a thin layer of thermo-expanding mat to avoid bypass phenomena in the region between the catalyst and the reactor wall, and a tubular sheath was inserted in correspondence of the catalytic bed axis to allow the temperature measurement: a K-type thermocouple was able to slide inside that sheath. The reactor was thermally insulated using a quartz wool layer in the void region between the external reactor wall and the electrical furnace employed to provide the necessary heat; external insulation at the outlet section of the reactor was achieved with a thicker layer of quartz wool. Further details about the experimental setup are reported in our previous work [30].

The main difference in the systems' representation is the catalyst shape. The powder catalyst and the aluminum foam can be considered as an axial symmetric domain; even though this represents an approximation, the assumption can be legitimized considering the powder packing and the random structure of the aluminum foam [32]. For this reason, they were both modeled through a 2D axial symmetric geometry, represented in Fig. 1, in which each element of the experimental setup was represented as an individual domain (numbered from 1 to 11). The exact representation of an open cell foam with a non-periodic structure is complicated, and the simulation is particularly burdensome, especially when involves the simultaneous analysis of fluid dynamic, heat transfer and – in particular – chemical reaction. A 2D analysis of a replicated segment of a non-periodic foam was reported by Kim et al. [34]. To simplify the calculus, both systems were considered as a pseudo-homogeneous medium. When this hypothesis is applied, COMSOL allows the definition of separate transport properties for the matrix and the fluid and no further considerations have to be made. In the sole case of the heat conduction coefficient, it is necessary to evaluate the effective transport property: due to the random structure of the foam and the random packing of the powder particles,

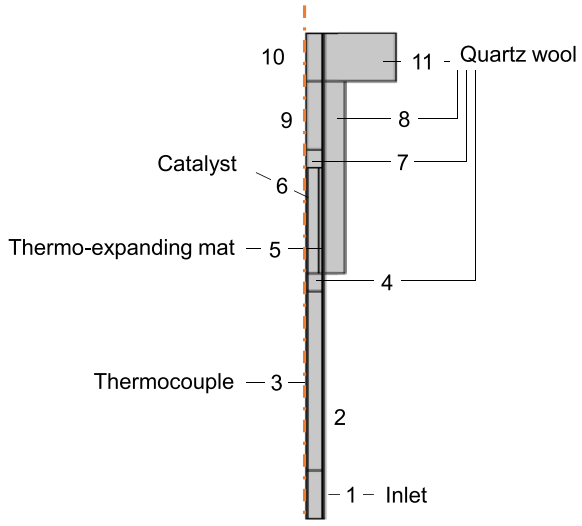

Fig. 1 – 2D geometry for the description of the powder catalyst and aluminum foam systems.

according with the software guidelines, it has been considered as an average of the two heat conduction coefficients, expressed as a power-law depending on the void fraction of the solid material (either powder catalyst or foam).

On the other hand, a 2D geometry and the hypothesis of a pseudo-homogeneous medium would not have been sufficient to represent the SiC monolith consistently, considering the channeling geometry which is characteristic of this structure (Fig. 2a). The three-dimensional representation of the monolith consisted of 52 channels, thus it would have been computationally burdensome and also time-consuming to model the whole domain: the smallest portion of the domain that can be considered without any approximation is a 45° slice, as it was possible to observe a 45° symmetry which is highlighted in Fig. 2b. The final representation of the SiC monolith structure is reported in Fig. 2c; the remaining sections of the system were described as well as in the 2D geometry (Supplementary materials, Fig. S1). The only difference was made for the catalyst domain, which was divided into 6a (the monolith structure) and 6b (the channels): to let COMSOL recognize the empty channels, it was necessary to define them as separate domains.

For the built-up of the system mesh, two different possibilities were considered: COMSOL provides, as discussed, different resolutions for meshing the domains, but it also allows to calibrate the mesh for (i) general physic, (ii) fluid dynamics, (iii) plasma and (iv) semiconductor. The different choice deals with the minimum size element, and in particular, the fluid dynamic mesh has always a higher resolution than the general physic mesh. Furthermore, the fluid dynamic mesh is constituted by higher resolution (i.e. smaller elements) at the inlet, the outlet, and the walls of the domain, which is where the calculus has to be more accurate. As a general criterion, it has been employed a general physic mesh for the domains which represent a solid, and a fluid dynamic mesh for the domains which represent the regions in which the gas flows, with different resolutions depending on the domain. Despite that, it was necessary to discretize the smaller solid

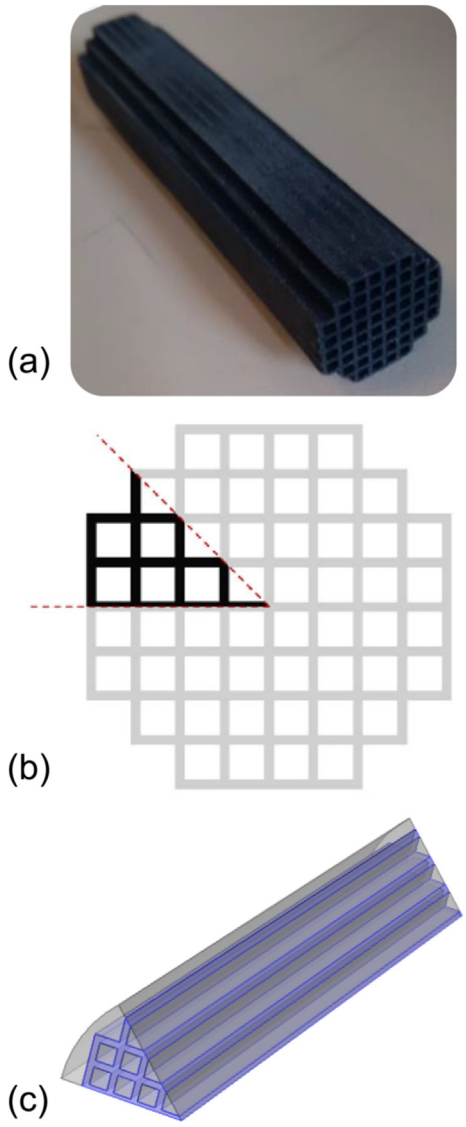

Fig. 2 – a) SiC monolith employed; b) front section of the monolith 3D geometry and representation of the 45°-slice; c) 3D visualization of the slice considered for modeling.

domains (the thermocouple sheath and the monolith structure) with a fluid dynamic mesh type. The type of mesh and resolution for each domain in both the geometries are given in supplementary materials, Table S1.

System definition in physics

As discussed, COMSOL solves complex problems through several physics. For the overall description of the three main transport phenomena, the momentum, the heat, and the mass balance equations were solved simultaneously employing three built-in physics (1. *Laminar flow*, 2. *Heat transfer in fluids*, and 3. *Transport of concentrated species*) and two multiphysics (*Nonisothermal flow* and *Reacting flow*) which allow the coupling of physics 1 and 2, and physics 1 and 3 respectively. The chosen physics are versatile since the *Laminar flow* physic allows the description of fluid flow both in free and porous media and the *Heat transfer in fluids* physic allows the description of solid domains too.

Fluid dynamic study

The fluid motion in free regions can be described using the Navier-Stokes equation for conservation of momentum (Eq. (1)) coupled with the continuity equation for conservation of mass (Eq. (2)), while, in porous media, the Brinkman equations (Eq. (3) to Eq. (5)) can describe the flow field.

$$\rho(\mathbf{u}\cdot\nabla)\mathbf{u} = \nabla\cdot\left[-p\mathbf{I} + \mu\left(\nabla\mathbf{u} + (\nabla\mathbf{u})^{T}\right) - \frac{2\mu}{3\varepsilon_p}(\nabla\cdot\mathbf{u})\mathbf{I}\right] \quad \text{Eq. 2}$$

$$\nabla\cdot(\rho\mathbf{u}) = 0 \quad \text{Eq. 3}$$

$$\frac{\rho}{\varepsilon_p}(\mathbf{u}\cdot\nabla)\frac{\mathbf{u}}{\varepsilon_p} = \nabla\cdot[-p\mathbf{I} + \mathbf{K}] - \left(\mu k^{-1} + \beta_F|\mathbf{u}| + \frac{Q_m}{\varepsilon_p^2}\right)\mathbf{u} \quad \text{Eq. 4}$$

$$\rho\nabla\cdot(\mathbf{u}) = Q_m \quad \text{Eq. 5}$$

$$\mathbf{K} = \left[\mu\frac{1}{\varepsilon_p}\left(\nabla\mathbf{u} + (\nabla\mathbf{u})^{T}\right)\right] - \frac{2}{3}\mu\frac{1}{\varepsilon_p}(\nabla\cdot\mathbf{u})\mathbf{I} \quad \text{Eq. 6}$$

To solve these equations, the software needs the definition of physical parameters and boundary conditions. The different materials which were associated with each domain are listed in Table 1 and they are all present in the COMSOL library materials: in most cases, the built-in physical parameters provided by COMSOL were found to be adequate to describe the system; despite that, some parameters were adjusted based on the specific materials employed in this work and they are reported in Table 2: the gas mixture values have been obtained based on the compositions, while the mats and the SiC monolith properties were provided by the supplier. In symbols, γ is the heat capacity ratio (C_p/C_v), C_p is the heat capacity at constant pressure, ε is the porosity, k is the permeability and K_T is the thermal conductivity. As boundary conditions, gas linear velocity $\mathbf{u_0}$ (normal inflow) was set at the inlet section (domain 1) based on the total flow rate employed in the experimental activity (1 NL min^{-1}, [30]), and atmospheric pressure was set at the outlet section (domain 10). At the wall and axis, in correspondence with the reactor wall and the thermocouple sheath, the no-slip condition was set.

Heat transfer study

As well as the fluid flow physic, heat transfer equations apply to fluid domains (Eq. (6) and Eq. (7)), solid domains (Eq. (11)), and porous media (Eq. (8) to Eq. (10)). For what concerns materials and physical parameters, the same considerations mentioned in 2.2.1 were applied. For what concerns the boundary conditions, numerous factors must be taken into account.

(i) At the inlet section (domain 1) the reactants are fed at room temperature: $T = T_R$
(ii) At the outlet section (domain 10), the outflow condition applies: $-\boldsymbol{n}\cdot\boldsymbol{q} = 0$
(iii) A constant temperature was set at the reactor wall (domains 1, 2, and 4) and at the external surface of the

Table 1 – Definition of materials per each domain.

Domain	Powder system	Foam system	SiC monolith system
1, 2, 9, 10	Gas mixture	Gas mixture	Gas mixture
4, 7	Gas mixture	Gas mixture	Gas mixture
	Glass wool board	Glass wool board	Glass wool board
6 (catalytic bed)	Gas mixture	Gas mixture	–
		Aluminum [solid, bulk]	–
6a (Sic monolith)	–	–	SiC (6H) - Silicon carbide
6b (Monolith channels)	–	–	Gas mixture
3	Steel AISI 4340	Steel AISI 4340	Steel AISI 4340
5	α-Al_2O_3 [solid, polycrystalline]	α-Al_2O_3 [solid, polycrystalline]	α-Al_2O_3 [solid, polycrystalline]
8, 11	Glass wool board	Glass wool board	Glass wool board

Table 2 – User-defined parameters.

Material	Parameters
Gas mixture	$\gamma = 1.48$
	$C_{p,mix} = 1014\ J\ kg^{-1}\ K^{-1}$
	$K_{T,mix} = 0.08\ W\ m^{-1}\ K^{-1}$
	$Mn_{mix} = 25.2\ g\ mol^{-1}$
Glass wool board	$\varepsilon = 0.92\ k = 1e\text{-}10\ m^2$
α-Al_2O_3 [solid, polycrystalline]	$K_T = 0.032\ W\ m^{-1}\ K^{-1}$
SiC (6H) - Silicon carbide	$K_T = 67\ W\ m^{-1}\ K^{-1}$

insulating wool corresponding to domain 8. The boundary condition applied is $T = T_{SP}$ (where T_{SP} is the set point temperature chosen as operating condition).

This boundary condition was made based on the experimental temperature control, which was performed through three different heating zones. A rendering of the experimental setup, together with a schematic view of the temperature control and the isothermal surfaces (highlighted in red) is given in supplementary materials, in Fig. S2. This system allowed to ensure an isothermal condition within the catalytic bed when the reaction does not occur (Fig. S3).

(iv) Despite the thermal insulation, the system cannot be considered perfectly adiabatic: for this reason, external natural convection has to be considered in domain 11.

Furthermore, the heat generated by the chemical reactions has to be considered in the catalytic bed volume (domain 6 for the 2D simulations and domains 6a and 6b for the 3D simulations). In this case, the software does not provide a built-in equation but allows the addition of a user-defined heat source. The overall heat generation was expressed as Eq. (12), where r_i and ΔH_i are related to the chemical reactions considered. Further details will be given in paragraph 2.2.3, in which the system characteristic reactions will be defined.

Fluid domains

$$\rho C_P \mathbf{u}\cdot\nabla T = \nabla\cdot(k\nabla T) + Q \quad \text{Eq. 7}$$

$$\mathbf{q} = -k\nabla T \quad \text{Eq. 8}$$

Porous media

$$(\rho C_P)_{eq}\mathbf{u}\cdot\nabla T = \nabla\cdot(k_{eq}\nabla T) + Q \quad \text{Eq. 9}$$

$$k_{eq} = \theta_P k_P + \theta_L k \quad \text{Eq. 10}$$

$$(\rho C_P)_{eq} = \theta_P(\rho C_P)_P + \theta_L \rho C_P \quad \text{Eq. 11}$$

Solid domain

$$\nabla\cdot(k\nabla T) + Q = 0 \quad \text{Eq. 12}$$

Heat generation

$$Q_{GEN} = \Delta H_3\cdot r_3 - \Delta H_2\cdot r_2 - \Delta H_1\cdot r_1 \quad \text{Eq. 13}$$

Mass transfer study

Mass balance equations are reported in Eq. (13) to Eq. (16), where ω_i is the mass fraction of the i component, j_i is the diffusive mass flux, M_n is the mean molar mass and D_i is the mass diffusivity of the i component.

$$\nabla\cdot j_i + \rho(\mathbf{u}\cdot\nabla)\omega_i = R_i \quad \text{Eq. 14}$$

$$j_i = -\left(\rho D_i^F \nabla\omega_i + \rho\omega_i D_i^F \frac{\nabla M_n}{M_n}\right)\mathbf{q} = -k\nabla T \quad \text{Eq. 15}$$

$$D_i^m = -\frac{1-\omega_i}{\sum_{k\neq i}\frac{x_k}{D_{ik}}} \quad \text{Eq. 16}$$

$$M_n = \left(\sum_i \frac{\omega_i}{M_i}\right)^{-1} \quad \text{Eq. 17}$$

In addition, the variation in the components' concentration derives from the chemical reactions occurring in the catalytic system. As widely recognized, three main reactions, the Sabatier reaction (r_3), the reverse water-gas shift (rWGS) reaction ($-r_2$), and the CO-methanation reaction ($-r_1$), can occur simultaneously [35].

$$(r_1): CH_4 + H_2O \rightleftarrows CO + 3H_2 \quad \Delta H_{298K} = +206\ kJ\ mol^{-1} \quad \text{Eq. 18}$$

$$(r_2): CO + H_2O \rightleftarrows CO_2 + H_2 \quad \Delta H_{298K} = -41\ kJ\ mol^{-1} \quad \text{Eq. 19}$$

$$(r_3): 4H_2 + CO_2 \rightleftarrows CH_4 + 2H_2O \quad \Delta H_{298K} = -165\ kJ\ mol^{-1} \quad \text{Eq. 20}$$

For these chemical equations, the reaction rate expression has been defined according to the Langmuir-Hinshelwood-like mechanism firstly proposed by Xu and Froment in their study about methane reforming and then widely employed to

describe these kinds of reacting systems [31,36]. The equations for the kinetic expressions implemented in COMSOL are then reported in Eq. (20), Eq. (21) and Eq. (22), for r_1, r_2 and r_3, respectively. The expression for the equilibrium constants are given in Ref. [36].

$$(r_1) = \frac{\frac{k_1}{p_{H_2}^{2.5}}\left[P_{CH_4}P_{H_2O} - \frac{P_{H_2}^3 P_{CO}}{k_{eq,1}}\right]}{DEN^2} \quad \text{Eq. 21}$$

$$(r_2) = \frac{\frac{k_2}{P_{H_2}}\left[P_{CO}P_{H_2O} - \frac{P_{H_2}P_{CO_2}}{k_{eq,2}}\right]}{DEN^2} \quad \text{Eq. 22}$$

$$(r_3) = \frac{\frac{k_3}{p_{H_2}^{3.5}}\left[P_{CH_4}P_{H_2O}^2 - \frac{P_{H_2}^4 P_{CO_2}}{k_{eq,3}}\right]}{DEN^2} \quad \text{Eq. 23}$$

$$DEN = 1 + K_{CH_4}p_{CH_4} + K_{CO}p_{CO} + K_{H_2}p_{H_2} + \frac{K_{H_2O}p_{H_2O}}{p_{H_2}} \quad \text{Eq. 24}$$

As boundary conditions, the molar fraction of each component in the feed stream was set ($y_{Ar} = 0.5$, $y_{CO2} = 0.1$ and $y_{H2} = 0.4$, [30]) while the molar fractions of the products were set to zero; the outflow condition corresponds to $-\boldsymbol{n}\cdot\rho D_i^m \nabla\omega_i = 0$.

Simulation conditions and parameters

As discussed, the computational analysis was at first conceived to be compared to the experimental results. For this reason, the first part of the work involves a set of six simulations that investigate the three different catalytic systems in two different temperature conditions. Basically, the models only differ for the boundary condition at the reaction wall and insulation layer, previously addressed as T_{SP}, which was considered to be 300 °C and 350 °C.

To add the chemical reactions kinetics to the computational study, a model has been developed to find the kinetic parameters which characterize the tested formulation. Pre-exponential factor and activation energy depend on the nature of the species which compose the catalyst: for this reason, the parameters have been optimized for the powder catalyst and considered the same for the structured catalysts.

The rate of formation/consumption for each specie considering the equations (17)–(19) can be expressed as follows (Eq. (24) to Eq. (28)):

$$CH_4 = -r_1 + r_3 \quad \text{Eq. 25}$$

$$CO = r_1 - r_2 \quad \text{Eq. 26}$$

$$H_2 = 3r_1 + r_2 - 4r_3 \quad \text{Eq. 27}$$

$$H_2O = -r_1 - r_2 + 2r_3 \quad \text{Eq. 28}$$

$$CO_2 = r_2 - r_3 \quad \text{Eq. 29}$$

The minimization of the objective function (Eq. (29)) which compare the molar fraction of the i-specie y_i obtained by the model and experimentally allowed the parameters optimization. The kinetic parameters found for each reaction are reported in Table 3. Comparing the activation energy of r_1 and r_3 it is possible to appreciate the high selectivity toward direct CO_2 methanation of our formulation compared to other literature catalysts [7].

$$f = \min\left(\sum_{i=1}^{n}\left(y_{i,exp} - y_{i,mod}\right)^2\right) \quad \text{Eq. 30}$$

Results and discussion

Fluid dynamic study

The study of the fluid dynamic behavior of the gas inside each system provides a visual analysis of the different velocity fields. The simulations results are here reported in a single condition, as there were no differences in the velocity profile determined by the change in T_{SP}. Fig. 3 represents the velocity field within the SiC monolith: Fig. 3a shows different sections perpendicular to the system axis, while Fig. 3b represents a single section parallel to the axis. As shown, the gas flows into the SiC monolith channels producing: (i) an increase in the local linear velocity, caused by the reduction of the cross-section, and (ii) a laminar flow velocity profile within each channel. An additional evaluation of the gas linear velocity profile was conducted within a singular channel, considering the velocity magnitude along parallel lines at the inlet of a selected channel (Fig. 3c): in Fig. 3d is possible to see that, after 1 mm inside the channel, the flow is completely developed and reaches a parabolic shape.

The velocity fields in the powder and in the foam catalytic bed are reported in Fig. 4. Because of the low void fraction, the powder catalyst ensures a flat velocity profile, reaching an almost plug-flow condition (Fig. 4a). The velocity profile within the foam structure is, of course, an approximation. Because of the chaotic structure of the catalyst, the local gas linear velocity might have different directions: in particular, at each point, the velocity vector is likely to have a non-null z component, as well as non-null r and θ components because of the tortuous flow [37]. Despite that, the overall gas motion is realized through the axial direction, meaning that the z component is prevailing. Due to the higher void fraction, the velocity profile within the foam system has a pseudo-parabolic shape in the inlet and outlet section of the catalytic bed, which is more evident than in the packed bed of powder. Nevertheless, a high friction is produced by the struts of the foam, which for this model is given as a function of the permeability, according to the work of Agostini et al. [38]. Due to the friction, the radial velocity profile is, again, almost plug-flow (Fig. 4b).

Table 3 – Kinetic parameters for the tested formulation.

	r_1	r_2	r_3
K_0 (mol Pa^n g_{cat}^{-1} s^{-1})	1.56e8	1.48	6.65e13
E_a (kJ mol^{-1})	150	71	229

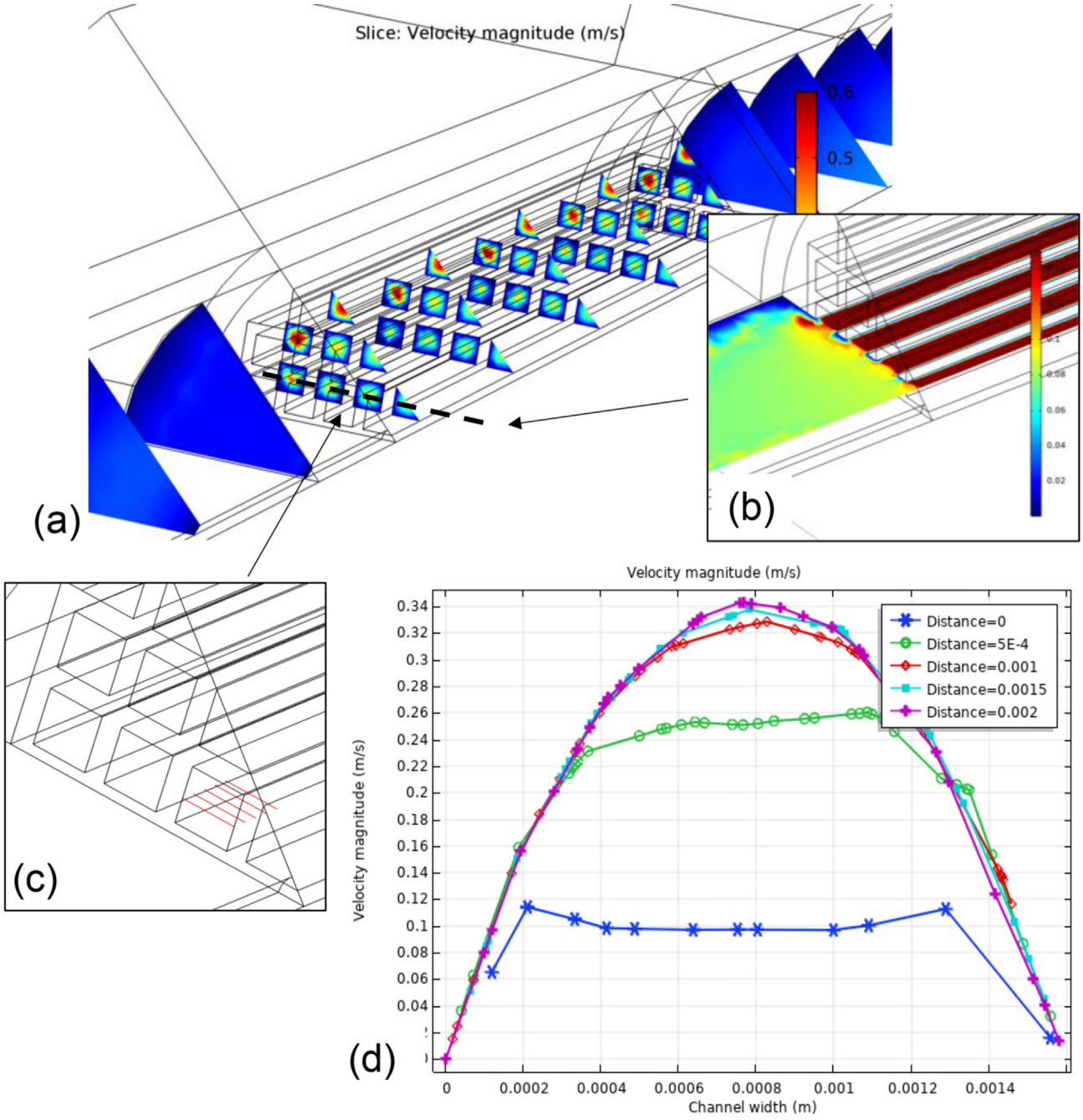

Fig. 3 – Velocity profile within the SiC monolith system: a) and b) 2D velocity profile; c) parallel lines in which the velocity field was evaluated to obtain d) a parametric study on the velocity profile within a channel.

Study of the heat transport phenomena

A comprehensive overview of the temperature profiles reached inside each system for a T_{SP} = 300 °C is given in Fig. 5. The temperature range and the color scale were liveried to have an immediate perception of the different thermal management within the catalysts: in each simulation, the heat generated by the chemical reactions clearly determines a temperature increase in the first part of the catalytic bed. This increase is remarkable in the case of the powder catalyst, while only slightly appreciable in the SiC monolith. In particular, it is possible to observe that in the SiC monolith heat is generated within each channel and transferred to the honeycomb structure and that heat dissipation is so high that in the outlet region of the catalytic bed the system is almost isothermal. Fig. 6 shows how the cold gas enters the monolith channels (x = 0) but when the reaction takes place the highest temperature is reached within the channel and transferred to the structure.

For what concerns the radial temperature profiles within the three catalytic systems, the comparison is displayed in Fig. 7. As can be observed, each system has its own thermal

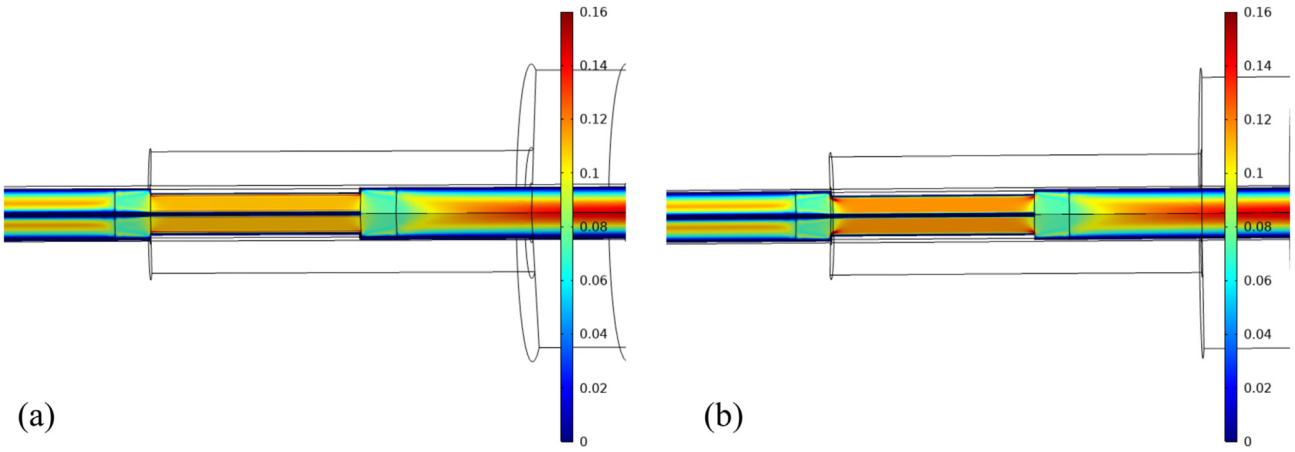

Fig. 4 – Velocity profiles (m/s) in: a) the powder catalyst system; b) the aluminum foam system.

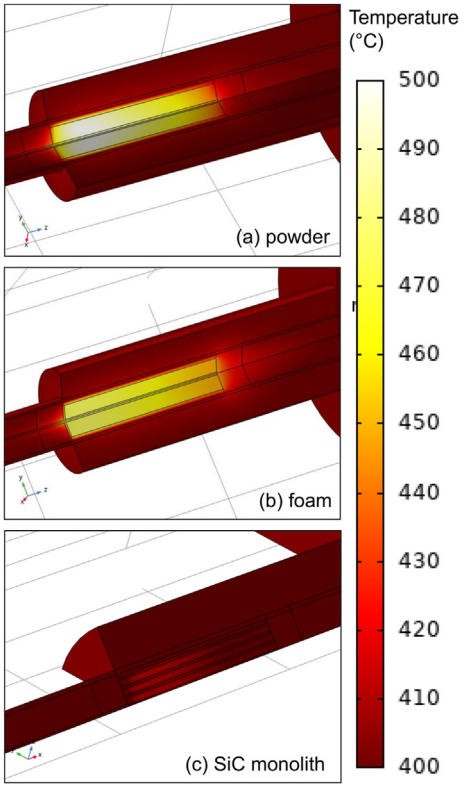

Fig. 5 – Temperature profile within the catalytic bed when $T_{SP} = 300$ °C and the catalyst is: a) powder shape; b) aluminum foam; c) SiC monolith.

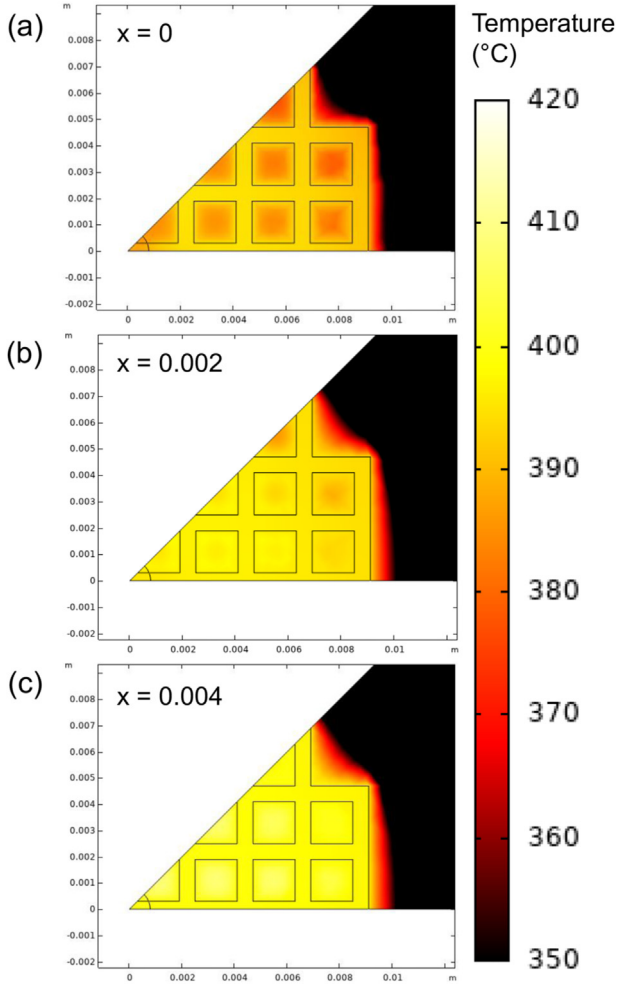

Fig. 6 – Temperature profiles in parallel section of the SiC monolith: x = 0, x = 0.002 m and x = 0.004 m.

entrance length. In the foam and powder systems, which have been approximated to a homogeneous medium, the average radial temperature at the inlet section is lower than the remaining catalytic bed, due to the continuous feed of the cold stream. On the other hand, in the SiC monolith, where the solid and gas phases have been clearly distinguished, it is possible to observe a peculiar profile (Fig. 7a). In the inlet region, at $z \leq 0.01$ (distance ≤ 0.01 in the graph) the temperature profile is parabolic within each channel and flat in correspondence with the solid wall of the monolith. The parabolic regions have a minimum when $z = 0$, according to the inlet of cold gas in the channel, and a maximum at $z \geq 0.05$ due to the occurrence of the exothermic reaction. Once the thermal balance is reached ($z \geq 0.05$), the radial temperature profile is almost flat.

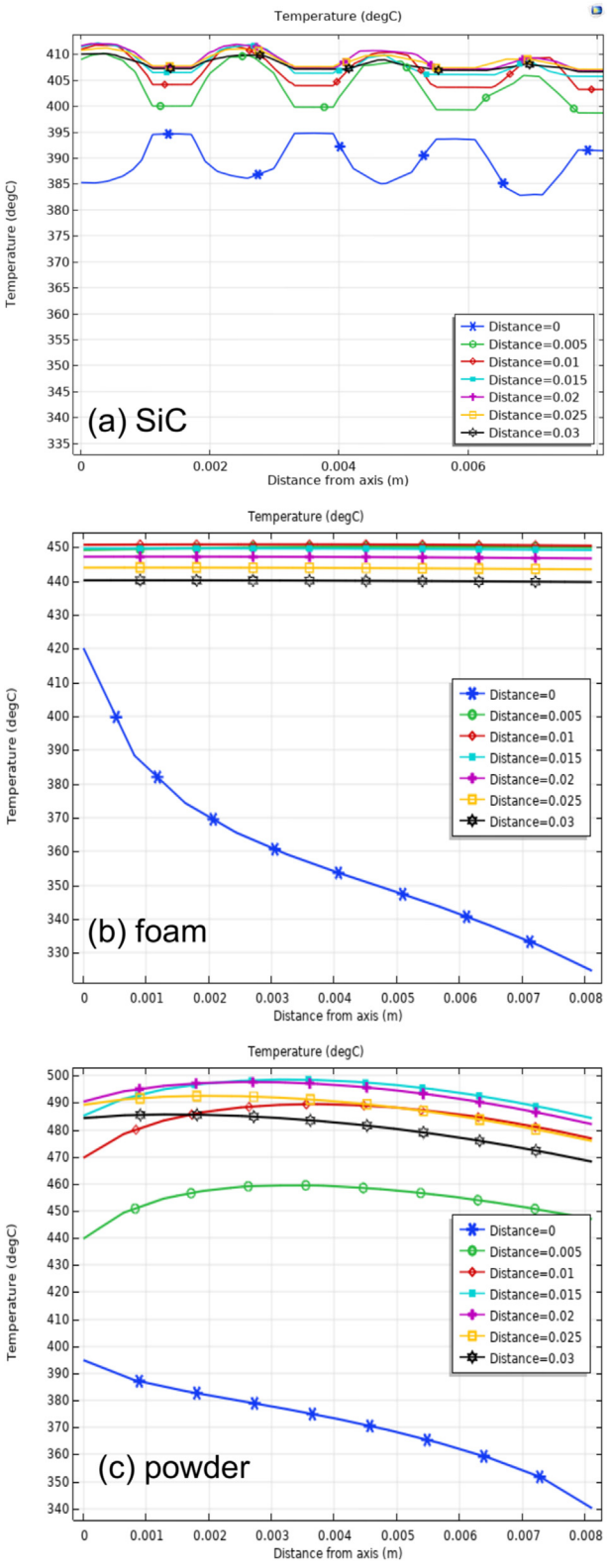

Fig. 7 – Radial temperature profiles: parametric study as a function of the distance from inlet. (a) SiC monolith; (b) aluminum foam; (c) powder catalyst.

In the foam (Fig. 7b), where heat conduction is faster, there is a strong increase in axial temperature at the inlet of the catalytic bed, but the temperature profile becomes immediately flat along the radial direction ($z \geq 0.05$). In the powder catalyst (Fig. 7c), because of the lower thermal conductivity of the solid, the flattening of the radial temperature profile requires a larger portion of the catalytic bed; furthermore, the temperature along the radial direction will not be as uniform as in structured catalysts. Indeed, a temperature gradient of about 10 °C is detected within the catalytic bed.

To highlight the mechanisms that produce the particular thermal profiles in the monolith, a further study was performed at the levels of the channels. The temperature profile within a single channel of the monolith was observed on the same lines defined to obtain the velocity profile (Fig. 3c) and the analysis gave very interesting results: in Fig. S4 is shown how the temperature profile develops within the channel. At the inlet of the channel, two effects compete: the continuous feeding of a relatively cold gas stream and the presence of hot SiC walls, heated by the reaction; these phenomena lead to a parabolic temperature profile with a minimum in correspondence to the channel axis. Since that the exothermic reaction takes place at the inlet of the catalytic bed, the temperature profile progressively flattens as the gas enters through the channel, until an almost flat temperature profile is reached. Then, the temperature increases within each channel because of the heat generation, reversing the parabolic shape, until the profile is flattered again by the heat exchange with the monolith. This result is particularly relevant, if considering the laminar velocity profile of the gas in the empty channels: it means that the channel width is small enough to ensure that the velocity field does not influence the radial temperature profile.

The remarks made for the case study in which $T_{SP} = 300$ °C are exactly the same that can be observed for the simulations with $T_{SP} = 350$ °C as a boundary condition. The temperature profiles obtained in this second condition gave similar results, thus leading to the same conclusions related to the heat management in the different systems: for completeness, these results are reported in supplementary materials (Figures S5, S6 and S7). The most relevant aspect of this study is the axial temperature profile along the catalytic bed: the results are reported in Fig. 8 for all the simulations, and temperature is displayed as a function of the axial position, where x = 0 corresponds to the inlet of the catalytic bed; negative x values correspond to the empty zone just before the catalytic bed. It is immediately clear the effect of the different thermal properties of the employed materials: structured catalyst offered a flatter thermal profile along the catalytic bed rather than the powder catalyst. In general, three main conclusions can be drawn from the observation of the axial profiles.

(i) Structured catalysts offer a flatter temperature profile than the powder catalysts, with the smoothest profile obtained with the SiC monolith.

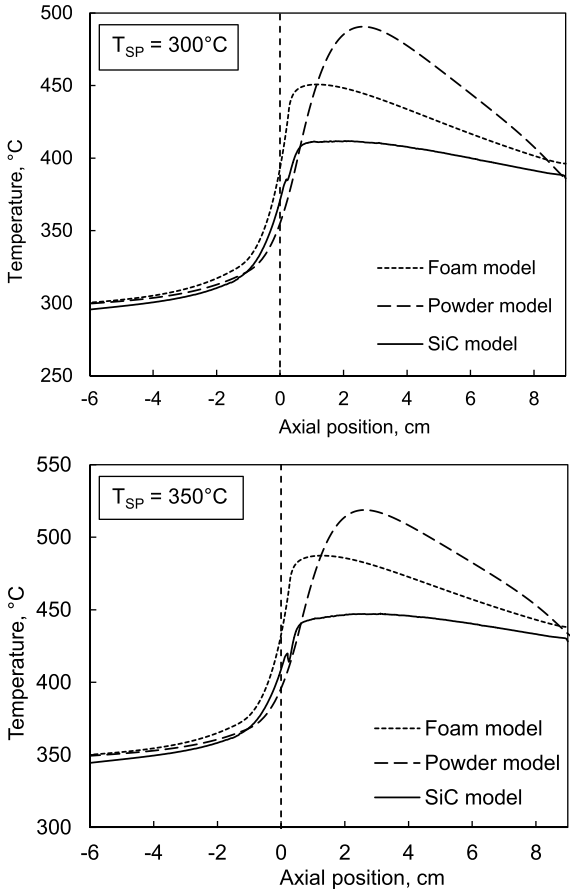

Fig. 8 – Axial profiles along the catalytic bed for the powder catalyst, the aluminum foam and the SiC monolith when $T_{SP} = 300$ °C and $T_{SP} = 350$ °C. Position x = 0 corresponds to the inlet section of the catalytic bed.

(ii) The catalytic bed has a lower average temperature in the systems with structured catalysts rather than in the system with the powder catalyst.
(iii) The temperature at the inlet section of the catalytic bed is higher than the set point temperature when a structured catalyst is employed.

For what concerns the first and second observations, this behavior is expected because the structured catalysts ensure a higher thermal conductivity, and this result has been widely reported in the literature [39–41]. Also, in the previous study we compared the effective thermal conductivity (thus considering the void fraction for the SiC monolith and the aluminum foam) to explain the flattest profile obtained with the SiC monolith which intrinsically has a lower thermal conductivity than aluminum. Instead, the third observation is peculiar, and it suggested the occurrence of a heat transfer from the core zone of the catalyst to the inner section: if we barely consider the axial position in which the maximum temperature is achieved, it can be said that, because of the temperature gradient, heat can be transferred in the axial direction both towards the inlet and the outlet zone. Despite that, the continuous flowing of a consistent amount of gas makes this observation less obvious, considering the convective heat flux determined by the gas motion in the system.

To determine the reasons for the temperature increase at the inlet of the catalytic bed, a comparative study of the heat fluxes has been conducted considering the powder catalyst system and the structured catalyst system. The aluminum foam was chosen for this study, to have the same geometrical representation, also considering that the thermal behavior of the two structured catalysts is very similar, with small discrepancies caused by the slightly different effective thermal conductivity. The fluxes analysis is reported in Fig. 9 for the powder and foam catalytic systems. From Fig. 9a it is possible to notice that in the powder catalyst system there is a prevalence of the convective heat flux (q_{conv}), while the conductive heat flux (q_{cond}) is barely negligible within the catalytic bed; a small amount of heat is transferred from the core of the catalytic bed to the inlet section through the thermocouple sheath (stainless steel) but this effect does not have a significant influence in the temperature profile. In the foam structure, instead, the situation is completely different: the conductive heat flux is way more effective, because of the higher thermal conductivity of the catalyst. This prevalence, especially in the inlet region, determined the rise in temperature in a section in which the reaction still does not take place. For this reason, if we consider the ratio q_{cond}/q_{conv} it comes out that this ratio, for the studied condition, is remarkably higher in the structured catalyst system rather than in the powder catalyst system.

Considering that q_{cond} depends on the temperature gradient and on the thermal conductivity, while q_{conv} depends on the temperature gradient and on the gas linear velocity, it is clear that the occurrence of the observed phenomenon is related to two main factors: a physical property of the employed catalyst (thermal conductivity) and an operating condition (gas linear velocity). This means that what was observed in this study is not reproducible in any case, as even if the physical properties of the catalysts would be the same, the operating conditions could involve a different gas linear velocity. This aspect becomes determining in the scale-up of this kind of systems: for a powder/pellet catalyst working with the same formulation and in the same space velocity conditions usually ensures performances comparable to the laboratory-scale results; for a structured catalyst instead, as other phenomena occur which enhance the reaction on small scale, further aspects have to be taken into account.

Mass transfer along with chemical reaction study

As discussed above, the kinetic parameters which characterize these reacting systems have been optimized through the Euler method. Employing these parameters, the Sabatier reaction (r_3, Eq. (22)) and the competitive reactions of reverse water-gs shift ($-r_2$, Eq. (21)) and CO methanation ($-r_1$, Eq. (20)) have been added to the COMSOL physics *Transport of concentrated species*. The computational evaluation of the reactions along the catalytic bed offers, in particular, to observe that the temperature profile influences the reactions kinetic: the evaluation of the reaction rate in the axial direction is shown in Fig. 10. Of course, there is a strong mutual influence of the

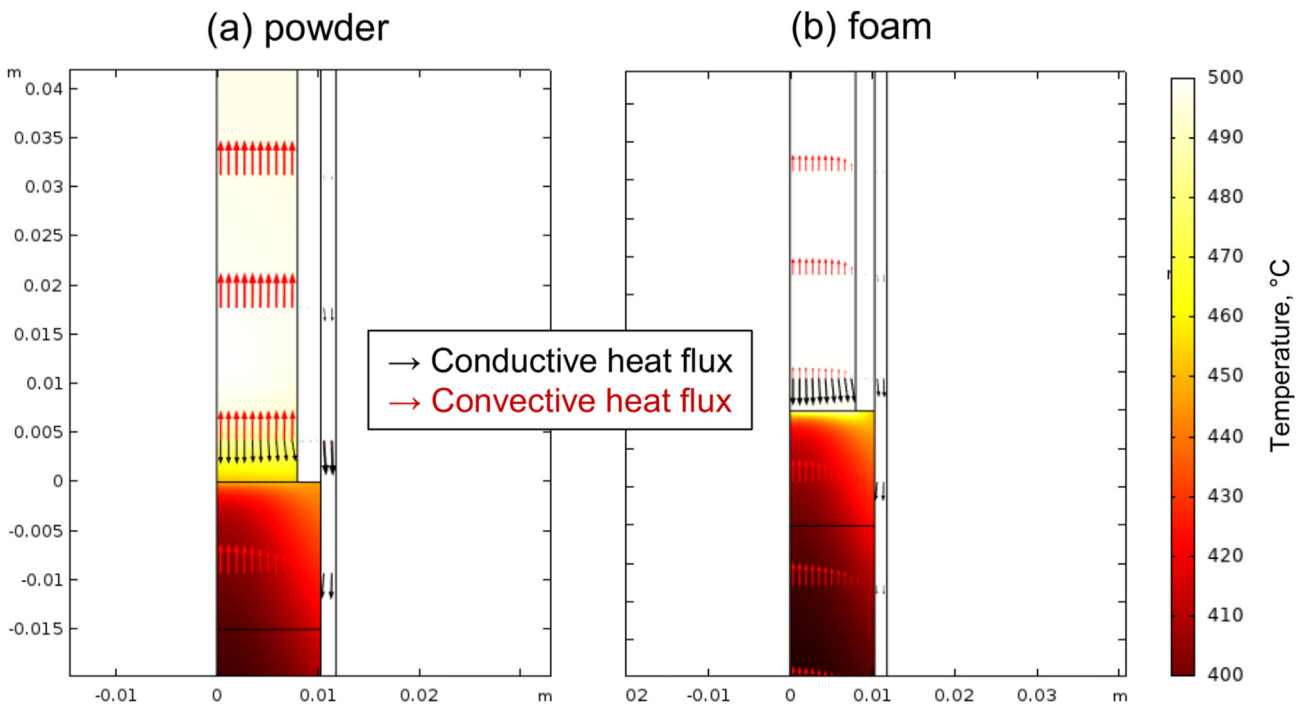

Fig. 9 – Conductive heat flux (black arrow) and convective heat flux (red arrow) evaluation in: a) powder catalyst; b) aluminium foam catalyst. (For interpretation of the references to color/colour in this figure legend, the reader is referred to the Web version of this article.)

reaction rate on the temperature and *vice-versa*: the higher the reaction rate, the higher the heat generation; on the other hand, in steady-state conditions, the retro-diffusion of heat towards the inlet section promotes the reactions kinetic and determines a more rapid increase of the reaction rates. This is particularly appreciable in the Sabatier reaction, whose kinetic behavior is strongly influenced by the temperature profile: as it is highlighted in Fig. 10a, the reaction starts quickly at the inlet section of the catalytic bed when a structured catalyst is employed, while in the powder catalyst the axial position in which the maximum reaction rate is reached coincides with the one in which the maximum temperature was observed. The r-WGS can be considered almost instantaneous for the three catalytic systems, even if it seems to occur to a more appreciable extent in the SiC monolith catalyst. This result is according to the analysis of the CO-methanation. This reaction can only occur in series with the r-WGS (which produces CO) and indeed it has a late start in the SiC monolith, where the r-WGS persists for a bigger portion of the catalytic bed. Furthermore, it is possible to observe that both the CO_2 and CO methanation reactions demonstrated to have a reaction rate that is remarkably higher in the SiC monolith rather than in the other catalytic systems. This can be explained considering that, at these high temperatures, there is not a kinetic limitation but, instead, there is a thermodynamic limitation: the SiC monolith system demonstrated to have the colder catalytic bed, so that the thermodynamic limitation has a lower influence.

Comparison with the experimental activity

To verify the validity of both the simulations and the experimental observations, the outcomes obtained with the model were compared to the experimental ones. The previous study involved not only the activity and selectivity of the different catalysts for the CO_2 methanation, but also the evaluation of the temperature profile which is produced along the catalytic bed by the occurrence of the chemical reaction, using the described sliding thermocouple.

A comparison between the experimental and the modeled temperature profiles is given in Fig. 11: as a first analysis, it can be observed the good fitting of the models to the respective experimental profile. The R^2 value for all the fittings was found to be higher than 0.94, and in particular the values are reported in Table 4.

The validity of the study was corroborated also by comparing the reaction achievements in terms of CO_2 conversion, CH_4 selectivity, CH_4 yield and CO yield. As it is possible to observe in Fig. 12, the model results are in good agreement with the experimental ones, and in particular the modeled and experimental values correspond within a 5% (or less) error range for all the catalytic systems and for both the set-point conditions considered in this study. The performances of these system were already discussed in the experimental study, but a comparison with a more recent literature highlights how the activity and selectivity achieved are still highly competitive [42–44].

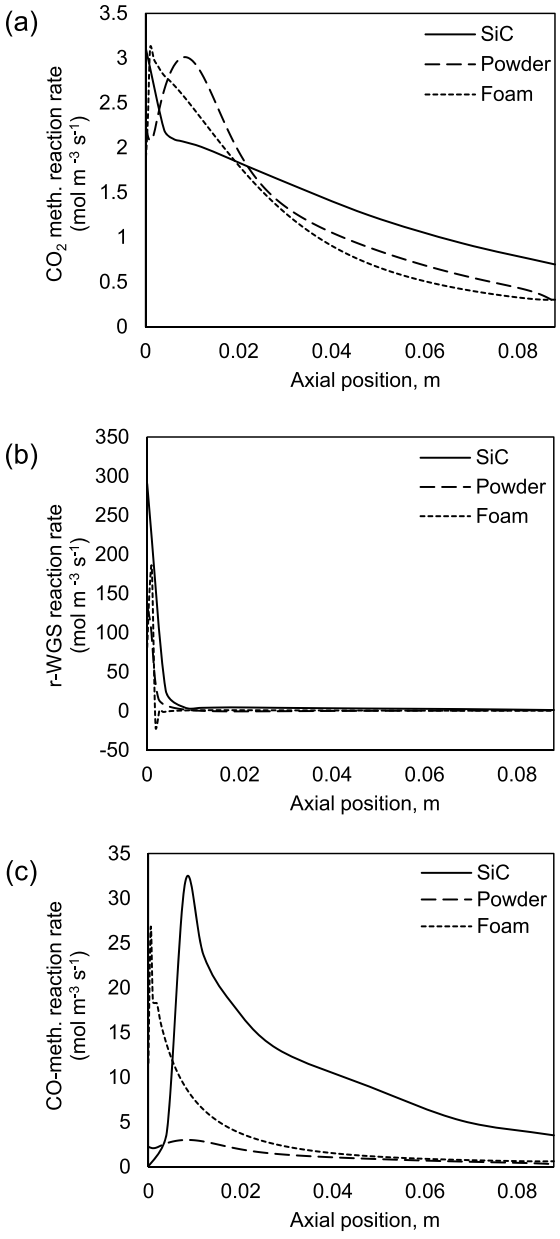

Fig. 10 – Reaction rate evolution along the axial direction within the SiC monolith, the aluminum foam and the powder catalyst for: a) the Sabatier reaction (CO_2 methanation), b) the reverse water-gas shift reaction (rWGS); c) the CO methanation reaction.

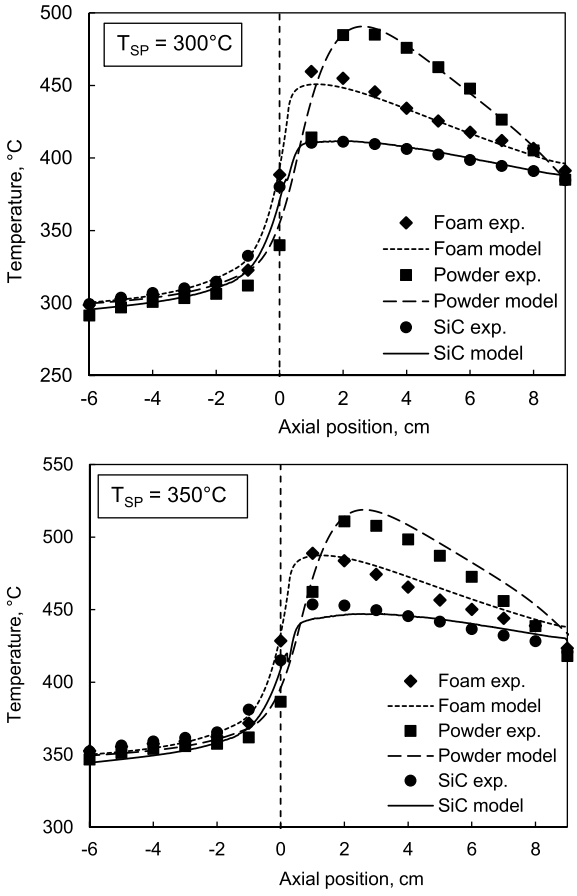

Fig. 11 – Comparison in temperature profiles between the experimental measurements and the model when T_{SP} = 300 °C and T_{SP} = 350 °C.

Table 4 – Calculated R^2 for all the models.

Model	Temperature, °C	R^2
SiC	300	0.989
SiC	350	0.948
Powder	300	0.952
Powder	350	0.963
Foam	300	0.994
Foam	350	0.985

Preliminary scale-up evaluations

In paragraph 3.2, it was briefly highlighted the possibility of incurring issues when scaling up a system constituted by structured catalysts, since peculiar phenomena were observed on small scale. An analysis of the failures in scale-up was already presented for monolith reactors for catalytic after-treatments [45] with a detailed enumeration of the dependencies of the similarity on several dimensionless parameter.

To support the considerations of paragraph 3.2 dealing with possible issues in the actual scale-up of the catalytic system, the model with the structured catalyst was simplified and studied under the hypothesis of adiabatic conditions, and then scaled up to a catalyst volume of 1 m^3. To provide the same contact time in such geometry, the gas linear velocity is forced to be one or two orders of magnitude higher than the one obtained in the laboratory scale, which was of the order of 10^{-2}. Adjusting the L/D ratio of the reactor to evaluate the effect of linear velocity, the profiles reported in Fig. 13 were obtained. The consequence of the increase in linear velocity is the decrease in temperature at the inlet of the catalytic bed, and, therefore, above a certain velocity value, the effect of retro-diffusion of heat is no longer appreciable.

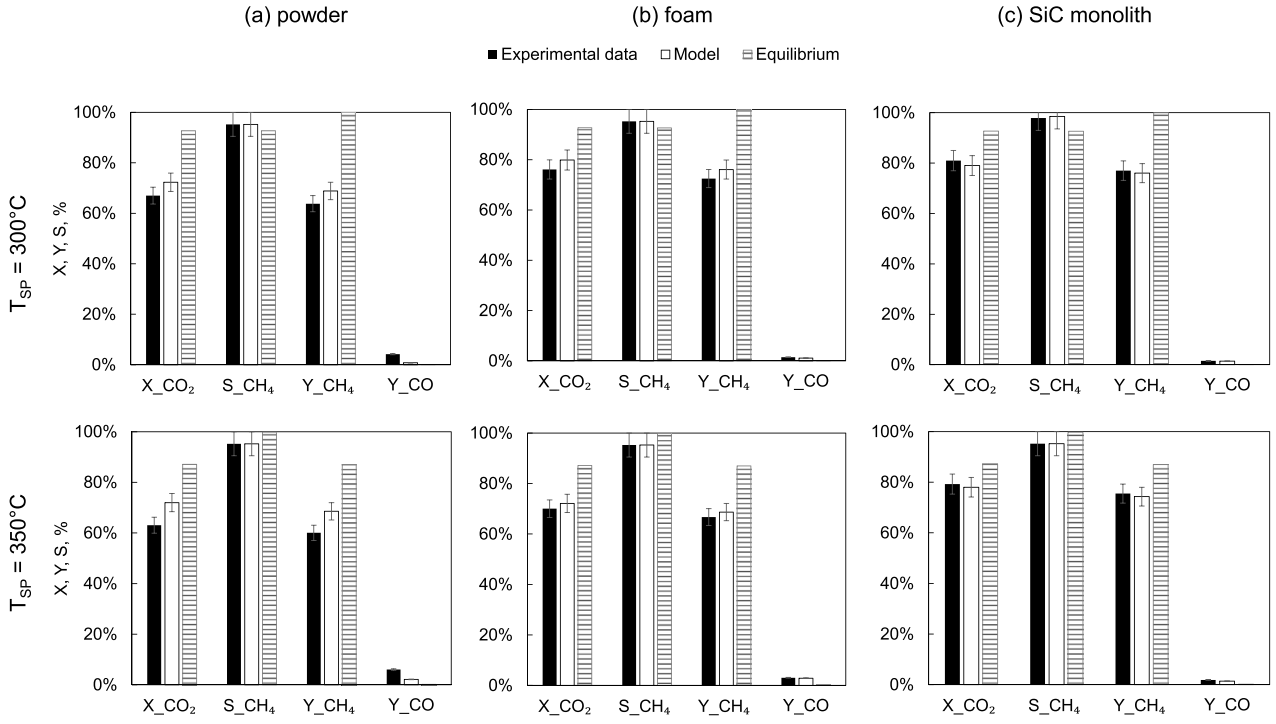

Fig. 12 – Comparison between the model and experimental results in terms of CO_2 conversion, CH_4 selectivity, CH_4 and CO yield.

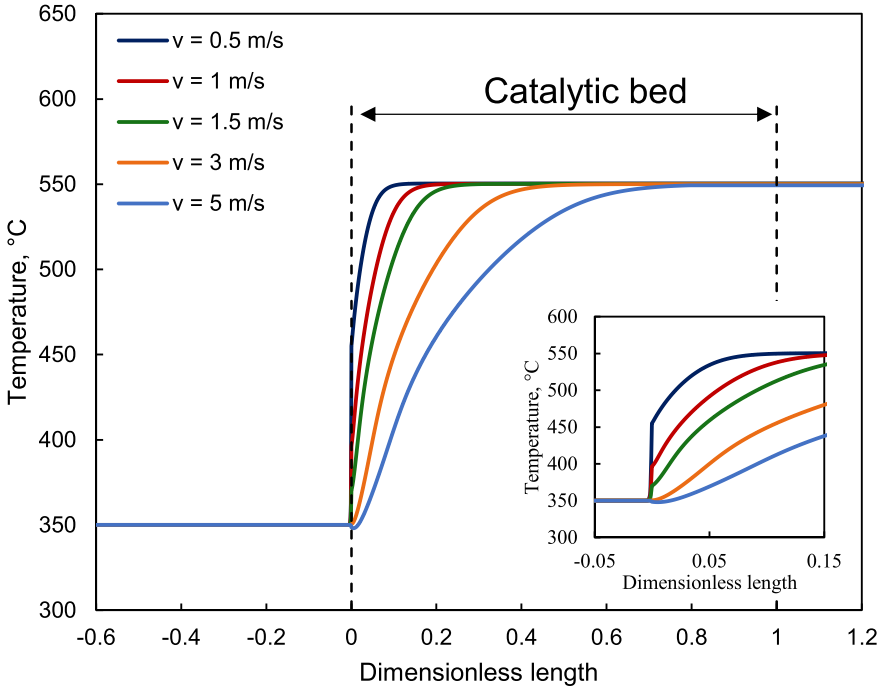

Fig. 13 – Temperature profile along the catalytic bed as a function of the gas linear velocity.

This is of course related to the fact that q_{cond} is always constant as it is independent from the reaction conditions, while q_{conv} progressively increases with the increase in linear velocity, thus the ratio q_{cond}/q_{conv} becomes lower until the conduction of heat along the structure and towards the inlet is completely negligible and inefficient if compared to the heat transferred through the convective mechanism.

This consideration leads to two possible solutions to maintain the beneficial effect of the employment of a structured catalyst in a scaled-up system: the first one is a modular

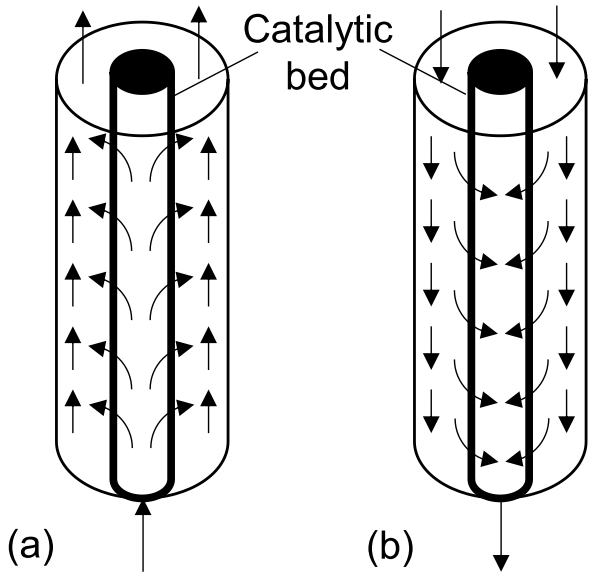

Fig. 14 – Scheme of radial geometry flow: a) centrifugal flow; b) centripetal flow.

solution in which the total flowrate is split, and the gas can reach slowly the catalytic bed; a second, promising possibility, is represented by the switch to a radial geometry. Both in the case of a centrifugal (Fig. 14a) or centripetal flow (Fig. 14b) this solution allows to substantially increase the surface that the gas flow faces within the system. This implies that, with the same aspect ratio and the same inlet gas flowrate, a radial geometry can ensure a linear gas velocity remarkably lower than the one which is realized in the linear geometry.

Conclusions

In this work, the CO_2 methanation was used as probe reaction in evaluating properties and peculiar behaviors of highly conductive structured catalysts employed in exothermic systems; the outcomes of the study were compared to the experimental observations made in a previous work, assessing the validity of the simulations results.

Through the computational study, the phenomena related to the thermal management in HCSC have been disclosed and the main drawback of their utilization has been highlighted.

The high conductivity of the structured catalysts was observed to have a more remarkable impact on the axial temperature profile rather than the radial one. Comparing the convective and conductive heat flux, it was found that in the inlet section of the catalytic bed, where the temperature gradient was at its maximum, a larger amount of heat was distributed via conduction in the opposite direction with respect to the gas flow. This effect allowed to increase the temperature at the inlet of the catalytic bed, promoting the reaction kinetically. Due to the dependency of the convective heat flux on the gas linear velocity, it was proven that the increase in gas linear velocity determines the loss of this advantage, since the convective heat flux is forced to rise and overcomes the heat conduction effect. This conclusion has a remarkable impact on the perspective of scaling up the application of structured catalysts to industrial systems, since that, with the conventional L/D ratios, the gas linear velocity unavoidably reaches higher order of magnitude. To put a step forward to the possible resolutions of this issue, the switch to a radial geometry configuration has been proposed at the end of this work. This possibility could be explored in future simulation studies, which would be captivating from the perspective of industrialization.

Declaration of competing interest

The authors declare that they have no known competing financial interests or personal relationships that could have appeared to influence the work reported in this paper.

Symbols

Greek

γ	heat capacity ratio (C_p/C_v)
ε	porosity (void fraction)
θ	porosity's complement to unity (1- ε)
ρ	density

Latin

C_p	heat capacity at constant pressure
D_i	mass diffusivity of the *i* component
E_a	Activation energy
j_i	diffusive mass flux of the *i* component
k	permeability
K_T	thermal conductivity
K_0	pre-exponential factor
M_n	mean molar mass
$\boldsymbol{n}$	normal vector
$\boldsymbol{q}$	heat flux
T	temperature
$\boldsymbol{u_0}$	normal inflow
ω_i	mass fraction of the *i* component
y_i	molar fraction of the *i* component

Appendix A. Supplementary data

Supplementary data to this article can be found online at https://doi.org/10.1016/j.ijhydene.2023.01.338.

REFERENCES

[1] Ruocco C, Coppola A, Picciotti G, Palma V. Experimental study of the oxidative steam reforming of fuel grade bioethanol over Pt–Ni metallic foam structured catalysts. Int J Hydrogen Energy 2022. https://doi.org/10.1016/j.ijhydene.2022.05.276. in press.

[2] Tronconi E, Groppi G, Visconti CG. Structured catalysts for non-adiabatic applications. Curr Opin Chem Eng 2014;5:55–67. https://doi.org/10.1016/j.coche.2014.04.003.

[3] Palma V, Barba D, Meloni E, Renda S, Ruocco C. Ultracompact biofuels catalytic reforming processes for distributed renewable hydrogen production. Stud Surf Sci Catal 2019;179:317–33. https://doi.org/10.1016/B978-0-444-64337-7.00017-3.
[4] Boffito DC, Van Gerven T. Process intensification and catalysis. Elsevier Inc.; 2019. https://doi.org/10.1016/b978-0-12-409547-2.14343-4.
[5] Van Gerven T, Stankiewicz A. Structure, energy, synergy, time-the fundamentals of process intensification. Ind Eng Chem Res 2009;48:2465–74. https://doi.org/10.1021/ie801501y.
[6] Huynh HL, Yu Z. CO2 methanation on hydrotalcite-derived catalysts and structured reactors: a review. Energy Technol 2020;8:1901475. https://doi.org/10.1002/ente.201901475.
[7] Sánchez A, Milt VG, Miró EE, Güttel R. Impact of heat transport properties and configuration of ceramic fibrous catalyst structures for CO2 methanation: a simulation study. J Environ Chem Eng 2022;10. https://doi.org/10.1016/j.jece.2022.107148.
[8] Di Stasi C, Renda S, Greco G, Palma V, González B, Manyà JJ. Wheat-straw-derived activated biochar as a renewable support of Ni-CeO2 catalysts for CO2 methanation. Sustain Times 2021;13:8939.
[9] Renda S, Di Stasi C, Manyà JJ, Palma V. Biochar as support in catalytic CO2 methanation : enhancing effect of CeO2 addition. J CO2 Util 2021;53:101740. https://doi.org/10.1016/j.jcou.2021.101740.
[10] Dou L, Yan C, Zhong L, Zhang D, Zhang J, Li X, et al. Enhancing CO2 methanation over a metal foam structured catalyst by electric internal heating. Chem Commun 2019;56:205–8. https://doi.org/10.1039/c9cc07525a.
[11] Renda S, Ricca A, Palma V. Study of the effect of noble metal promotion in Ni-based catalyst for the Sabatier reaction. Int J Hydrogen Energy 2020. https://doi.org/10.1016/j.ijhydene.2020.05.093.
[12] Lin Y, Zhang W, Machida H, Norinaga K. CFD simulation of the Sabatier process in a shell-and-tube reactor under local thermal non-equilibrium conditions: parameter sensitivity and reaction mechanism analysis. Int J Hydrogen Energy 2022;47:15254–69. https://doi.org/10.1016/j.ijhydene.2022.03.029.
[13] FarisAbadi A, Kazemeini M, Ekramipooya A. Investigating a HEX membrane reactor for CO2 methanation using a Ni/Al2O3 catalyst: a CFD study. Int J Hydrogen Energy 2022. https://doi.org/10.1016/j.ijhydene.2022.06.290.
[14] Meloni E, Martino M, Iervolino G, Ruocco C, Renda S, Festa G, et al. The route from green H2 production through bioethanol reforming to CO2 catalytic conversion: a review. Energies 2022;15. https://doi.org/10.3390/en15072383.
[15] Italiano C, Drago Ferrante G, Pino L, Laganà M, Ferraro M, Antonucci V, et al. Silicon carbide and alumina open-cell foams activated by Ni/CeO2-ZrO2 catalyst for CO2 methanation in a heat-exchanger reactor. Chem Eng J 2022;434. https://doi.org/10.1016/j.cej.2022.134685.
[16] González-Castaño M, Baena-Moreno F, Carlos Navarro de Miguel J, Miah KUM, Arroyo-Torralvo F, Ossenbrink R, et al. 3D-printed structured catalysts for CO2 methanation reaction: advancing of gyroid-based geometries. Energy Convers Manag 2022;258. https://doi.org/10.1016/j.enconman.2022.115464.
[17] Navarro JC, Centeno MA, Laguna OH, Odriozola JA. Ru–Ni/MgAl2O4 structured catalyst for CO2 methanation. Renew Energy 2020;161:120–32. https://doi.org/10.1016/j.renene.2020.07.055.
[18] Cimino S, Cepollaro EM, Lisi L, Fasolin S, Musiani M, Vázquez-Gómez L. Ru/ce/ni metal foams as structured catalysts for the methanation of co2. Catalysts 2021;11:1–15. https://doi.org/10.3390/catal11010013.
[19] Ratchahat S, Sudoh M, Suzuki Y, Kawasaki W, Watanabe R, Fukuhara C. Development of a powerful CO2 methanation process using a structured Ni/CeO2 catalyst. J CO2 Util 2018;24:210–9. https://doi.org/10.1016/j.jcou.2018.01.004.
[20] Vita A, Italiano C, Pino L, Laganà M, Ferraro M, Antonucci V. High-temperature CO2 methanation over structured Ni/GDC catalysts: performance and scale-up for Power-to-Gas application. Fuel Process Technol 2020;202:106365. https://doi.org/10.1016/j.fuproc.2020.106365.
[21] Danaci S, Protasova L, Lefevere J, Bedel L, Guilet R, Marty P. Efficient CO2 methanation over Ni/Al2O3 coated structured catalysts. Catal Today 2016;273:234–43. https://doi.org/10.1016/j.cattod.2016.04.019.
[22] Iwaniszyn M, Gancarczyk A, Gąszczak A, Kołodziej A. Structured intra-tubular catalyst carrier for highly exothermic processes: modelling and CFD study. Int J Heat Mass Tran 2021:175. https://doi.org/10.1016/j.ijheatmasstransfer.2021.121357.
[23] Giani L, Groppi G, Tronconi E. Mass-transfer characterization of metallic foams as supports for structured catalysts. Ind Eng Chem Res 2005;44:4993–5002. https://doi.org/10.1021/ie0490886.
[24] Fukahori S, Koga H, Kitaoka T, Nakamura M, Wariishi H. Steam reforming behavior of methanol using paper-structured catalysts: experimental and computational fluid dynamic analysis. Int J Hydrogen Energy 2008;33:1661–70. https://doi.org/10.1016/j.ijhydene.2007.12.063.
[25] Ghasemzadeh K, Zeynali R, Basile A, Iulianelli A. CFD analysis of a hybrid sorption-enhanced membrane reactor for hydrogen production during WGS reaction. Int J Hydrogen Energy 2017;42:26914–23. https://doi.org/10.1016/j.ijhydene.2017.06.152.
[26] Pashchenko D. Effect of the geometric dimensionality of computational domain on the results of CFD-modeling of steam methane reforming. Int J Hydrogen Energy 2018;43:8662–73. https://doi.org/10.1016/j.ijhydene.2018.03.183.
[27] Chen L, Pannala S, Broekhuis R, Gautam P, Gu T, West D, et al. Three-dimensional CFD simulation of pattern formation in a shallow packed-bed reactor for oxidative coupling of methane. Chem Eng J 2020;400:125979. https://doi.org/10.1016/j.cej.2020.125979.
[28] Shah M, West D, Balakotaiah V. Analysis of temperature patterns in shallow-bed autothermal catalytic reactors. Chem Eng J 2022;437:135027. https://doi.org/10.1016/j.cej.2022.135027.
[29] Balakotaiah V, Christoforatou EL, West DH. Transverse concentration and temperature nonuniformities in adiabatic packed-bed catalytic reactors. Chem Eng Sci 1999;54:1725–34. https://doi.org/10.1016/S0009-2509(99)00013-5.
[30] Ricca A, Truda L, Palma V. Study of the role of chemical support and structured carrier on the CO2 methanation reaction. Chem Eng J 2019;377:120461. https://doi.org/10.1016/J.CEJ.2018.11.159.
[31] Xu J, Froment GF. Methane steam reforming, methanation and water-gas shift: I. Intrinsic kinetics. AIChE J 1989;35:88–96. https://doi.org/10.1002/aic.690350109.
[32] Palma V, Goodall R, Thompson A, Ruocco C, Renda S, Leach R, et al. Ceria-coated replicated aluminium sponges as catalysts for the CO-water gas shift process. Int J Hydrogen Energy 2021;46:12158–68. https://doi.org/10.1016/j.ijhydene.2020.04.065.
[33] Renda S, Ricca A, Palma V. Precursor salts influence in Ruthenium catalysts for CO2 hydrogenation to methane.

Appl Energy 2020;279:115767. https://doi.org/10.1016/j.apenergy.2020.115767.
[34] Kim M, Kim M, Hosseini S, Jeong J, Kim KC. PIV measurement of turbulent flow characteristics inside an open-cell metal foam replica. Opt Laser Eng 2022;158. https://doi.org/10.1016/j.optlaseng.2022.107143.
[35] Renda S, Ricca A, Palma V. Precursor salts influence in Ruthenium catalysts for CO2 hydrogenation to methane. Appl Energy 2020;279:115767. https://doi.org/10.1016/j.apenergy.2020.115767.
[36] Chein R-Y, Yu C-T, Wang C-C. Numerical simulation on the effect of operating conditions and syngas compositions for synthetic natural gas production via methanation reaction. Fuel 2016;185:394–409. https://doi.org/10.1016/j.fuel.2016.07.123.
[37] Vespertini A, Torre A Della, Montenegro G, Onorati A, Nova I, Tronconi E, et al. CFD analysis on the optimization of POCS performances under randomical transformations : a bridge with open-cell foams. Chem Eng Sci 2023;267:118309. https://doi.org/10.1016/j.ces.2022.118309.
[38] Agostini E, Boccardo G, Marchisio D. An open-source workflow for open-cell foams modelling: geometry generation and CFD simulations for momentum and mass transport. Chem Eng Sci 2022;255:117583. https://doi.org/10.1016/j.ces.2022.117583.
[39] Balzarotti R, Ambrosetti M, Beretta A, Groppi G, Tronconi E. Investigation of packed conductive foams as a novel reactor configuration for methane steam reforming. Chem Eng J 2020;391:123494. https://doi.org/10.1016/j.cej.2019.123494.
[40] Fratalocchi L, Groppi G, Visconti CG, Lietti L, Tronconi E. Adoption of 3D printed highly conductive periodic open cellular structures as an effective solution to enhance the heat transfer performances of compact Fischer-Tropsch fixed-bed reactors. Chem Eng J 2020;386:123988. https://doi.org/10.1016/j.cej.2019.123988.
[41] Palma V, Pisano D, Martino M, Ricca A, Ciambelli P. High thermal conductivity structured carriers for catalytic processes intensification. Chem Eng Trans 2015;43:2047–52. https://doi.org/10.3303/CET1543342.
[42] Fan WK, Tahir M. Investigating the product distribution behaviour of CO2 methanation through thermodynamic optimized experimental approach using micro/nano structured titania catalyst. Energy Convers Manag 2022;254:115240. https://doi.org/10.1016/j.enconman.2022.115240.
[43] Cui Y, Chen B, Xu L, Chen M, Wu Ce, Qiu J, et al. CO2 methanation over the Ni-based catalysts supported on the hollow ZSM-5 zeolites: effects of the hollow structure and alkaline treatment. Fuel 2023;334:126783. https://doi.org/10.1016/j.fuel.2022.126783.
[44] Yuan S, Ma P, Yang Y, Shen X, Pan H, Li Z, et al. Highly active sunlight-driven Co2 methanation catalyst: design of the interfacial structure. SSRN Electron J 2022;335:126855. https://doi.org/10.2139/ssrn.4217354.
[45] Gu T, Balakotaiah V. Impact of heat and mass dispersion and thermal effects on the scale-up of monolith reactors. Chem Eng J 2016;284:513–35. https://doi.org/10.1016/j.cej.2015.09.005.